INVESTIGATION ON AN ACTIVE WINGLET INFLUENCING THE WAKE OF A LARGE TRANSPORT AIRCRAFT

Alexander Allen, Christian Breitsamter
Institute of Aerodynamics, Technische Universität München
Boltzmannstr. 15, D-85748 Garching, Germany

Keywords: *Wake Vortex, Large Transport Aircraft, Passive Influencing, Wind Tunnel, Experiment*

Abstract

The results of a wind tunnel investigation on the wake vortex evolution behind a half model of a four engined large transport aircraft in high lift configuration, with and without influencing by winglet tabs, are presented. The wake is measured by means of advanced hot–wire anemometry up to 5.6 spans downstream of the model. Results obtained include vorticity and turbulence intensity fields. The measured data is processed in order to evaluate the influence of the winglet tabs on the vortex decay rate.

Nomenclature

AR	Aspect ratio
b	Wing span
c_L	Lift coefficient
f	Frequency
HTV	Horizontal Tail Plane Vortex
INV	Inboard Nacelle Vortex
OFV	Outboard Flap Vortex
ONV	Outboard Nacelle Vortex
s	Semi span ($s = b/2$)
Tu_z	Turbulence intensity in z-direction
U_∞	Freestream velocity
u, v, w	Axial, lateral and vertical velocity
$\overline{u}, \overline{v}, \overline{w}$	Mean axial, lateral and vertical vel.
u', v', w'	Fluctuation part of u, v and w
WLV	Winglet Vortex
WRP	Wing Reference Point
WTV	Wing Tip Vortex

x, y, z	Coordinates in x-, y- and z-direction
x^*	Non dimensional distance in x-direction $\left(x^* = \frac{x}{b} \right)$
y^*	Non dimensional distance in y-direction $\left(y^* = \frac{y}{s} \right)$
z^*	Non dimensional distance in z-direction $\left(z^* = \frac{z}{s} \right)$
α	Angle of attack
δ	Deflection angle of winglet tabs
τ^*	Non dimensional time $\left(\tau^* = x^* \frac{16 c_L}{\pi^4 AR} \right)$
ξ	Non dimensional axial vorticity

1 Introduction

The increasing air traffic and the growing difficulties in expanding airports and runways burdens the capacities at major airports around the world. In order to counter act this development, aircraft size is increased. The minimum distance between two aircraft on approach or take–off is primarily driven by the weight and therewith by the size of the two aircraft [2]. To meet the requirements of growing air traffic a reduction of the separation distances, without reducing the level of safety already obtained today, would lead to a relief at hub airports. Larger and larger aircraft can only disburden the bottleneck if their separation distances are not increased in comparison to large transport aircraft today.

The trailing vortices of the preceding aircraft are a potential safety issue for the following aircraft [6]. Depending on the position and the flight path of the following aircraft, an upwash or a

downwash, causing high structural loads, as well as an induced rolling moment, with the risk of loosing control, can occur.

All across the world scientist are investigating the behaviour of wake vortices and their interaction and decay in order to reduce separation distances to a minimum [1] [4] [5]. Different passive and active devices have been tested to reduce the overall vorticity or to increase dissipation, which would lead to a faster decay [3] [7] [8] [9] [10] [11].

This paper focuses on the influence of tabs at the trailing edge of a large winglet on a large transport aircraft.

2 Experimental Set–Up

The investigation was conducted in the wind tunnel C of the Institute of Aerodynamics at Technische Universität München (TUM) using a large transport aircraft configuration and employing advanced hot–wire anemometry.

2.1 The Wind Tunnel

The wind tunnel C is of closed–return type and has a long range test section of 21m length, which corresponds to 5.6 spans downstream of the model. The wind tunnel has a cross section of $1.8m \times 2.7m$. The ceiling is adjustable in order to control the pressure gradient along the test section. The turbulence level at the nozzle exit is less than 0.5%. The wind tunnel C is equipped with a traversing system to which the hot–wire probe is mounted.

2.2 The Model

A half model of a typical large transport aircraft was used for this investigation. The model is made of aluminium and is equipped with fully adjustable flaps, slats, aileron and horizontal tail plane (see Figure 1).

The engine nacelles are through–flow nacelles and they have no exhaust jet simulation devices. The model also has no landing gear. The model was tested in landing configuration as

stated in Table 1, where the positions of the movable control surfaces are listed.

Slat	Inboard	26.5^o
	Midboard	26.5^o
	Outboard	30.0^o
Flap	Inboard	26.0^o
	Outboard	26.0^o
Aileron		5.0^o
Horizontal Tail Plane		-10.0^o

Table 1 Settings

The model was tested with the "original" large winglet, which later was replaced by the winglet containing the movable tabs for active and passive influencing. The new winglet is made of titan and was manufactured by the Institute of Aerodynamics at TU München especially for this investigation. Figure 2 shows the new winglet with the tabs. It has approximately the same size as the original winglet and in order to supply sufficient space for the tab actuators a thicker airfoil than for the original winglet was chosen, namely the NACA65A012 airfoil. The winglet is equipped with two separately moveable trailing edge tabs, which can be deflected up to an angle of ±20 statically or dynamically up to a frequency of $100Hz$. Figure 2 also shows the motor case, a tilted cylinder at the lower side of the winglet. It was not possible to incorporate the motor in the wing, which made the external housing necessary. The influence of the tilted cylinder on the flow field will be discussed later.

2.3 The Measuring Equipment

A triple wire probe operated by a multi–channel constant temperature anemometer was used. The wires are platinum plated and have a diameter of $5\mu m$ and a length of approximately $1.25mm$. A sampling rate of $3000Hz$ (Nyquist frequency $1500Hz$) and a sampling time of $6.4s$ were chosen. This corresponds to 19200 measuring values per wire and survey point. The output signal of the anemometer bridges are low–pass filtered at $1000Hz$. The anemometer output signals are converted into time dependent velocity compo-
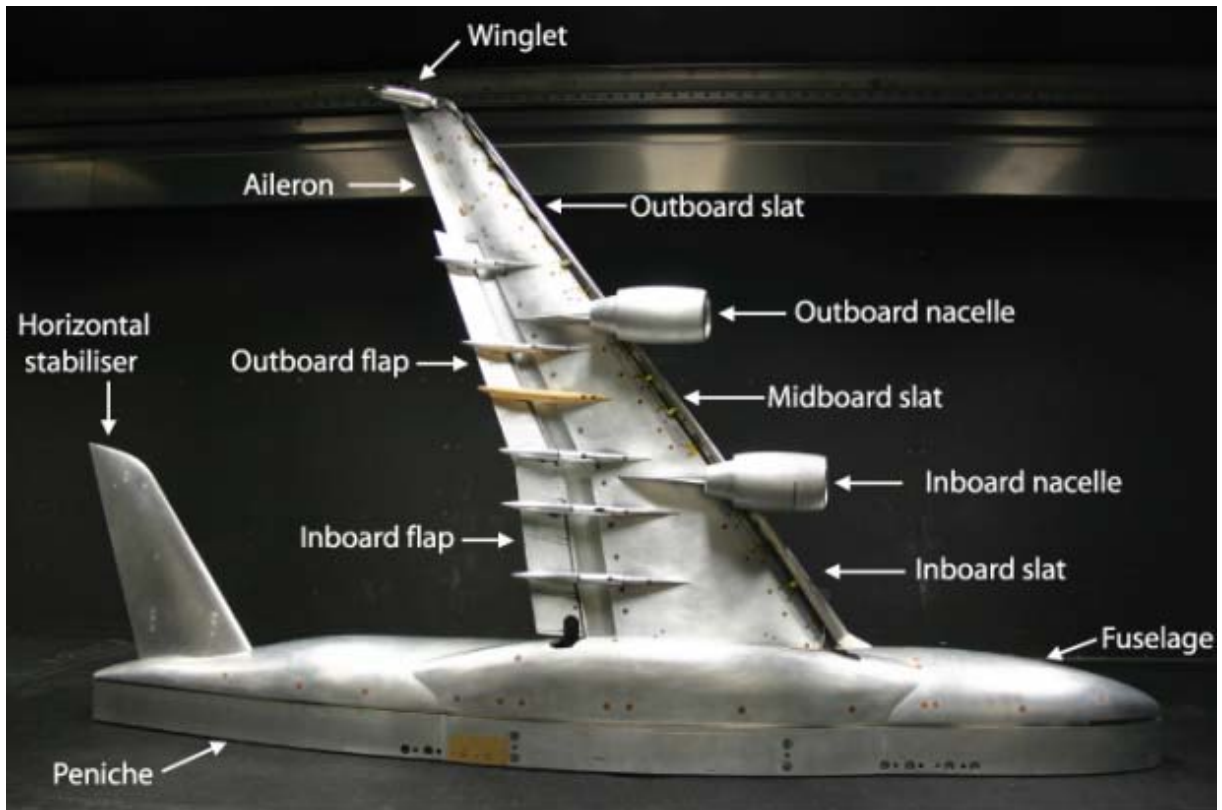
Fig. 1 Half model in wind tunnel C
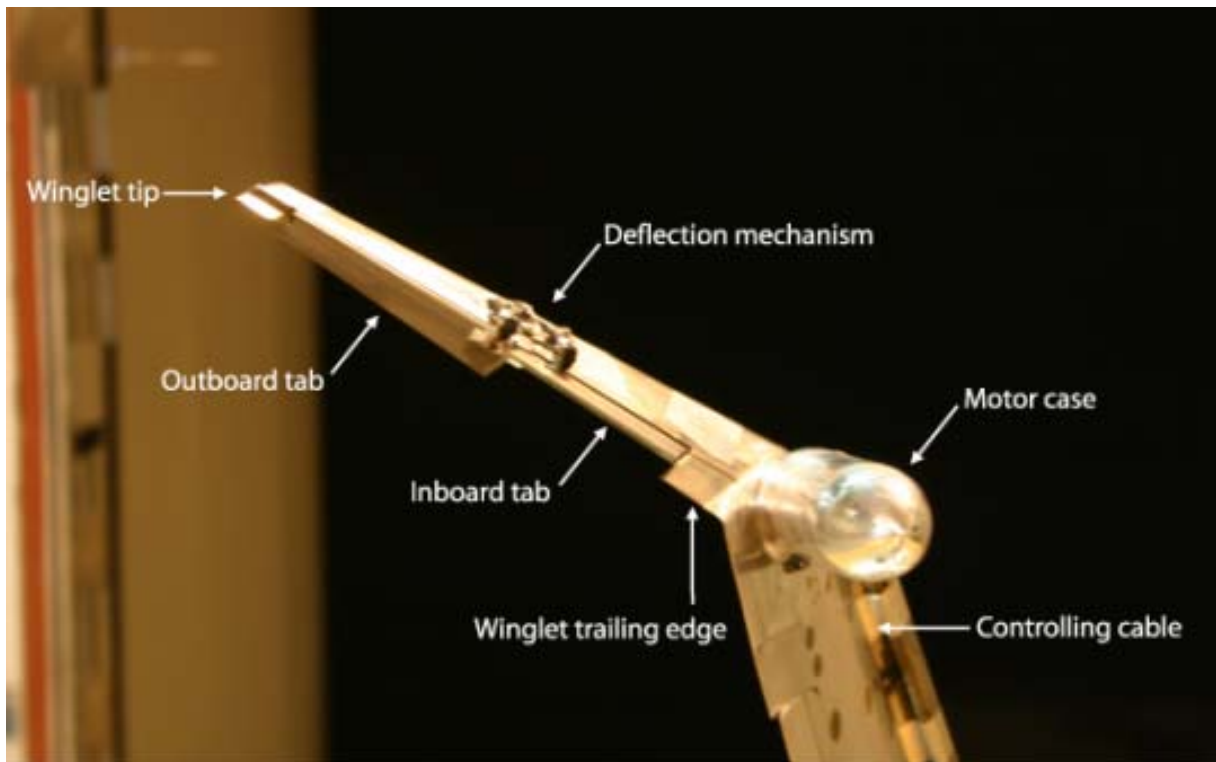
Fig. 2 The new winglet with tabs

nents u, v and w using a look–up table previously obtained from the velocity and angle dependent calibration of the hot–wire probe.

3   Results

The investigations were all performed at a velocity of $25 m/s$ with the corresponding Reynolds number being $514,000$ based on the mean aerodynamic chord. The angle of attack for the original winglet was chosen to be $\alpha = 7.0^o$ and for the new winglet $\alpha = 6.5^o$ in order to keep the lift coefficient constant at $c_L = 1.43$.

Inspecting the surface flow with tufts showed attached flow is present on wing and horizontal tail plane and therefore no transition strips were attached to the model.

The wake vortex was measured in planes perpendicular to the freestream direction at distances x^* between 0.02 and 5.6 downstream of the wing reference point (WRP). The WRP is the trailing edge at the winglet tip at an angle of attack of $\alpha = 0.0^o$. The x-direction is orientated in lengthwise and the y-direction in spanwise direction. The z-direction is perpendicular to x and y. In regions of high gradients, i.e. in the regions of vorticity layers and vortex cores, the survey points are closely spaced, whereas outside these regions spacing is enlarged.

The results are presented as plots of axial vorticity (ξ) and turbulence intensity fields in z-direction (Tu_z), which is approximately perpendicular to the wing plane. ξ is described by equation 1 and Tu_z by equation 2.

$$\xi = \frac{s}{U_\infty} \left(\frac{\partial \overline{w}}{\partial y} - \frac{\partial \overline{v}}{\partial z} \right) \qquad (1)$$

$$Tu_z = \sqrt{\frac{\overline{w'^2}}{U_\infty^2}} \qquad (2)$$

3.1   Results without Influencing

In order to quantify the influence of the new winglet on the flow field, a detailed investigation was conducted on both winglets without passive or active influencing.

3.1.1   The Original Winglet

The axial vorticity distribution in the plane at $x^* = 0.37$ ($\tau^* = 0.011$) is shown in Figure 3 and the corresponding turbulence intensities in Figure 4.
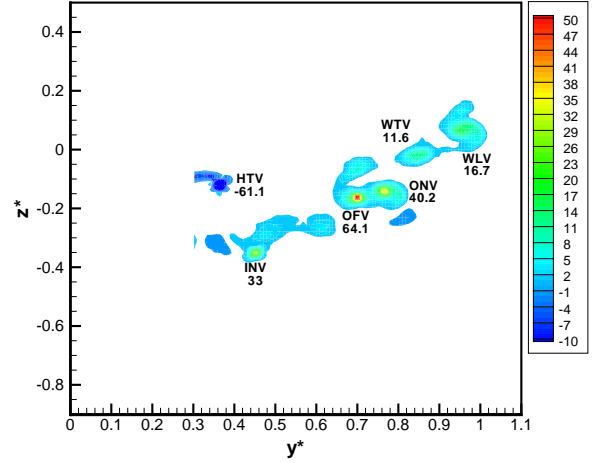
Fig. 3 Vorticity distribution for the baseline configuration at $x^* = 0.37$

Note, that the vorticity levels $-1.0 < \xi < 1.0$ are blanked in all figures showing vorticity distributions, in order to clarify the positions of the vortices. Turbulence intensities $Tu_z < 0.02$ are also blanked to show the vortex sheet emanating from the wing more clearly.
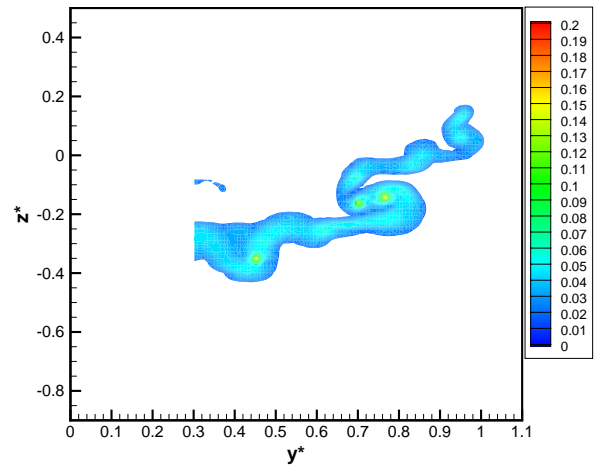
Fig. 4 Tu_z distribution for the baseline configuration at $x^* = 0.37$

In Figure 3 the dominating near field vortices are marked and their vorticity peaks are stated.

Six main vortices can be identified, namely from outboard to inboard, the Winglet Vortex (WLV), the Wing Tip Vortex (WTV), the Outboard Nacelle Vortex (ONV), the Outboard Flap Vortex (OFV), the Inboard Nacelle Vortex (INV) and the Horizontal Tail Plane Vortex (HTV). Note that the HTV has negative vorticity and is therefore counter–rotating in comparison to the other five vortices. The horizontal tail plane is adjusted for negative lift due to trimmed flight and, therefore, the HTV exhibits negative vorticity. Figure 4 clearly shows the vortex sheet emanating from the wing and slightly above, the vortex sheet shed at the horizontal tail plane. The two strongest vortices in Figure 3 are the ONV and the OFV and the s–shape of the vortex sheet in that region indicates, that the two vortices have already turned 180° around each other (see Figure 4). Higher turbulence levels are visible in the regions of high vorticity. Figure 3 also shows several smaller vortices in between the six dominating vortices. These vortices are caused by slathorns, flap track fairings and other geometric discontinuities of the wing.

The axial vorticity distribution in the plane furthest downstream at $x^* = 5.60$ ($\tau^* = 0.164$) is shown in Figure 5 and the corresponding turbulence intensity in Figure 6.
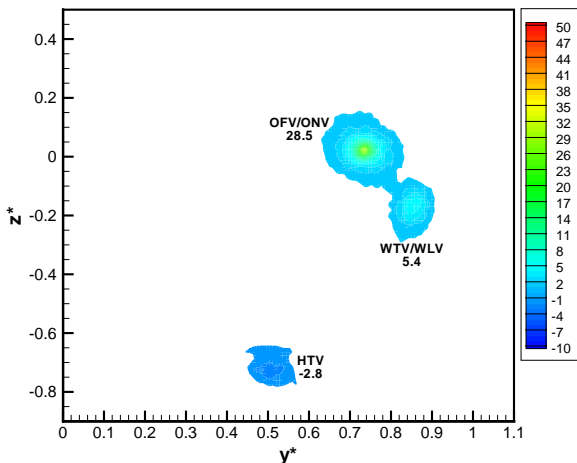
Fig. 5 Vorticity distribution for the baseline configuration at $x^* = 5.60$

Figure 5 shows the three remaining vortices of the extended near field. The strongest one
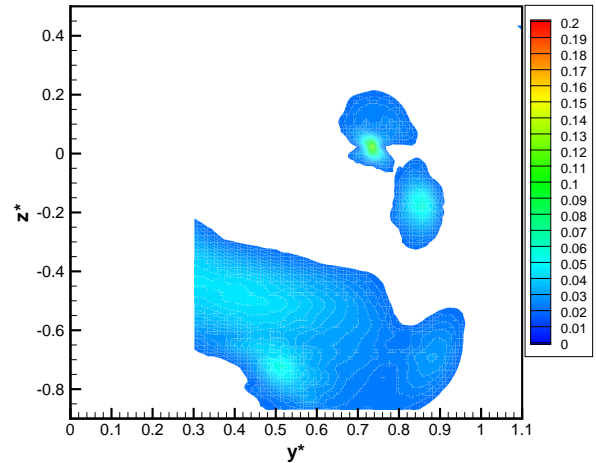
Fig. 6 Tu_z distribution for the baseline configuration at $x^* = 5.60$

is formed by the merging of the OFV with the ONV and the other one by the merging of the WTV and the WLV. The HTV is also still visible, but its vorticity has almost decayed completely. The INV has decayed, which will be shown later. The vortex sheet of the OFV/ONV and the WTV/WLV are also connected, which means that merging will occur soon. In comparison to Figure 3 the two strongest vortices have rotated around each other approx. 270° and the overall vorticity has decreased clearly. Again increased turbulence levels at the positions of the vortices are visible in Figure 6. The vortex sheet emanating from the wing is not visible as such any more. Furthermore the two strongest vortices are not connected to this sheet anymore, whereas the HTV is now fully embedded in the sheet.

3.1.2 The Winglet With Tabs

The measurements were repeated for the new winglet with tabs. To compare these results with the data obtained from the original winglet, the tabs were fixed at $\delta_{lower} = \delta_{upper} = 0^o$.

Figure 7 shows the axial vorticity distribution in the plane closest to the model at $x^* = 0.02$ ($\tau^* = 0.0006$) and Figure 8 the corresponding turbulence intensity field. As the measuring plane is upstream of the horizontal tail plane, the HTV is missing and with it, the entire turbulence sheet emanating from the horizontal tail plane.
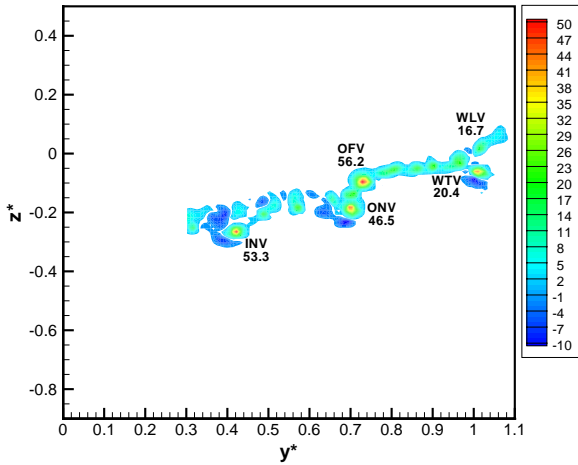
Fig. 7 Vorticity distribution for the configuration with the new Winglet at $x^* = 0.02$
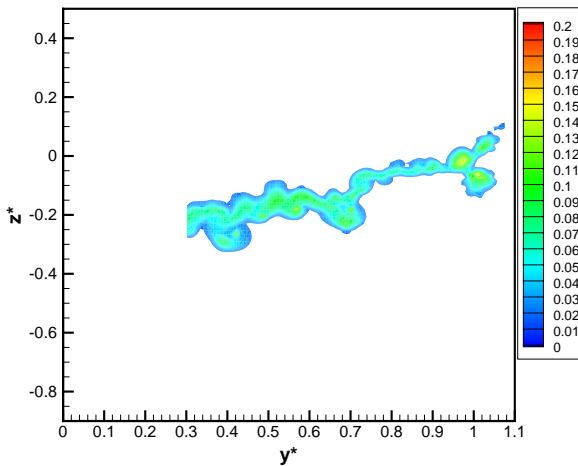
Fig. 8 Tu_z distribution for the configuration with the new Winglet at $x^* = 0.02$

Five dominating vortices can be seen in Figure 7, namely the WLV, WTV, OFV, ONV and INV. They are accompanied by several other vortices, which are all weaker and are caused by the geometry details of the high lift wing configuration, as mentioned previously. Figure 7 also shows a vortex just outboard of the WTV at the wing tip. This is caused by the tilted cylinder on the lower side of the winglet housing the motor to drive the tabs. This vortex will quickly merge with the WLV as will be shown later. Figure 8 shows the turbulence sheet just behind the wing. The nacelles can clearly be seen as bulge in the sheet at approximately $y^* = 0.4$ and $y^* = 0.7$. Just

outboard of the bulge caused by the outboard nacelle at $y^* = 0.7$ a jump in the turbulence sheet can be observed. This is caused by the outer edge of the flap. Inboard of this point the flow is washed down stronger by the almost fully extended flaps. Outboard of this point the flow is washed down by the ailerons extended at $\xi = 5^o$. At the tip the shape of the winglet can be recognized in the turbulence intensity plot. A similar picture can be seen in the vorticity plot in Figure 7.

The following two figures show the vorticity distribution and the turbulence intensity field at $x^* = 0.37$ ($\tau^* = 0.011$) (see Figure 9 and 10).
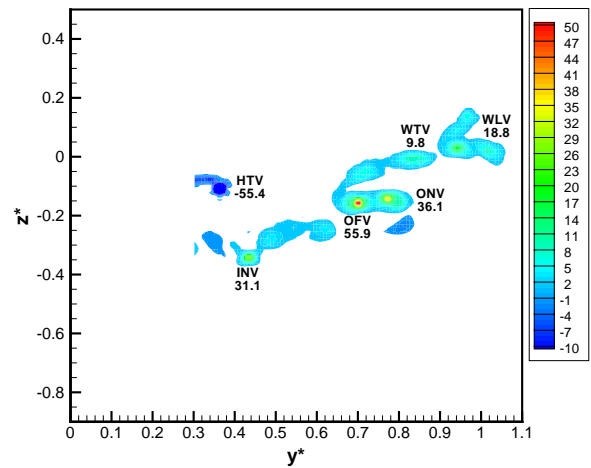
Fig. 9 Vorticity distribution for the configuration with the new Winglet at $x^* = 0.37$

Comparing the figures with the results obtained for the baseline configuration (see Figure 3 and 4) differences are visible in the area of the wing tip. Apart from these differences the flow field appears to be the same. The peak vorticity values and turbulence intensity levels differ slightly due to slightly changed outboard wing loading. Note, that the lift coefficient is the same for the baseline configuration and the configuration with the new winglet.

The differences at the winglet were expected as the airfoil of the winglet was changed and the tilted cylinder is not neglectable. Nevertheless the flow field topology is still appropriate for the investigations on active winglets. There are still six vortices dominating the flow field and Figure
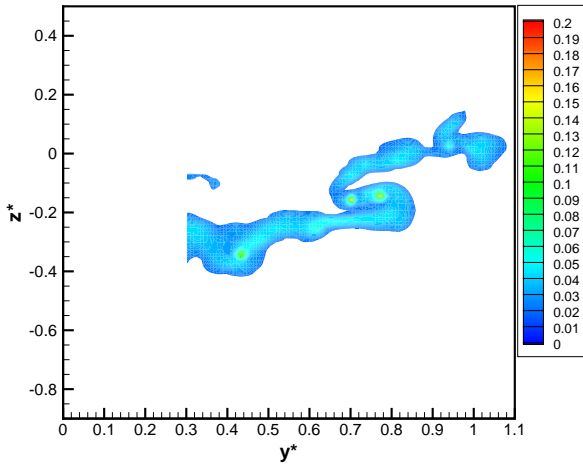
Fig. 10 Tu_z distribution for the configuration with the new Winglet at $x^* = 0.37$
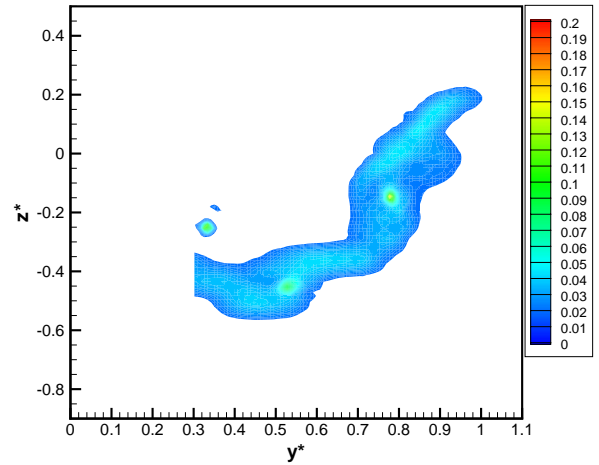
Fig. 12 Tu_z distribution for the configuration with the new Winglet at $x^* = 1.00$

10 also shows the s–shape in the turbulence sheet indicating the 180° rotation of the ONV and OFV around their roll–up center.

Continuing downstream to $x^* = 1.00$ ($\tau^* = 0.029$) Figure 11 and 12 show the vorticity distribution and turbulence intensity field, respectively.

Fig. 11 Vorticity distribution for the configuration with the new Winglet at $x^* = 1.00$

Different than for the baseline configuration at $x^* = 0.37$ (see Figure 3) the WTV for the configuration with the new winglet is connected to the OFV and ONV in Figure 9. It is assumed, that the WTV is rolled up into the OFV/ONV rather than into WLV as with the baseline con-

figuration. The v–shaped vorticity distribution around the WLV in Figure 9 rolls up into the WLV in Figure 11. So at $x^* = 1.00$ only four vortices are left, with the OFV/ONV/WTV being the strongest with positive rotation. The vorticity peaks for all vortices are reduced and the core diameters have increased. Figure 12 shows the turbulence sheet of the wing still connected and the sheet emanating from the horizontal tail plane almost reduced to a single vortex, namely the HTV.

Figure 13 illustrates the vorticity distribution and Figure 14 the turbulence intensity for the new winglet configuration at $x^* = 2.00$ ($\tau^* = 0.059$).

Fig. 13 Vorticity distribution for the configuration with the new Winglet at $x^* = 2.00$

Fig. 14 Tu_z distribution for the configuration with the new Winglet at $x^* = 2.00$

Fig. 15 Vorticity distribution for the configuration with the new Winglet at $x^* = 3.00$

All vortices have rotated counter clockwise around the roll–up center, a point in the vicinity of the OFV/ONV/WTV. The vorticity peak values have decreased even further with the core diameters only slightly reduced. The turbulence sheet from the wing has split into several bits, leaving the OFV/ONV/WTV and the WLV only weakly linked. The HTV is now embedded in the turbulence field from the wing–fuselage area as illustrated in Figure 14. It can also clearly be seen, that the turbulence sheet is deformed by the counter clockwise rotation of the vortices in comparison to the shape upstream of $x^* = 2.00$.

Figure 15 shows the axial vorticity distribution in the plane at $x^* = 3.00$ ($\tau^* = 0.088$) and Figure 16 the corresponding turbulence intensity field.

The counter clockwise rotation has continued and the vorticity peaks have decreased further, except for the OFV/ONV/WTV, where the vorticity peak increased slightly. The turbulence sheet is also further deformed.

The following two figures show the vorticity distribution and the turbulence intensity field at $x^* = 4.00$ ($\tau^* = 0.117$) (see Figure 17 and 18).

The WLV and INV have further decreased both in vorticity and turbulence intensity. The counter clockwise rotation is also still ongoing. The WLV is not visible in the turbulence intensity distribution, but in the vorticity distribution. The
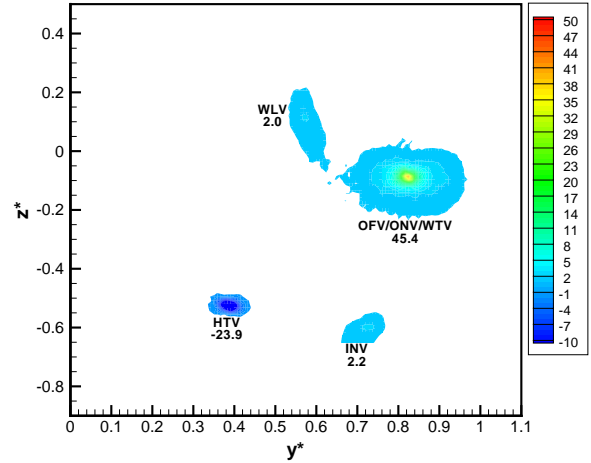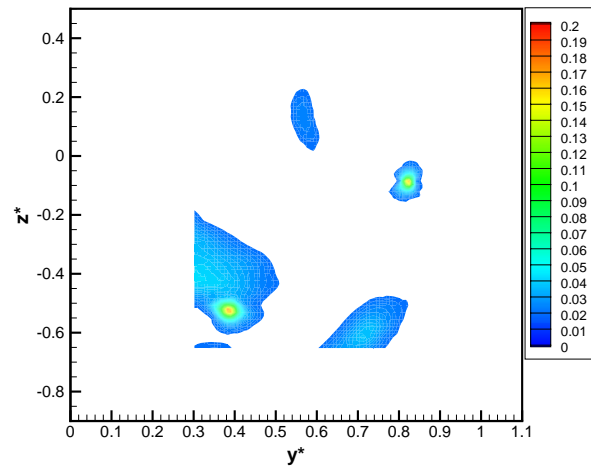
Fig. 16 Tu_z distribution for the configuration with the new Winglet at $x^* = 3.00$

reason for this still needs to be examined closer.

Continuing to the furthest downstream measuring plane at $x^* = 5.60$ ($\tau^* = 0.164$) Figure 19 and 20 show the vorticity distribution and turbulence intensity field, respectively.

The WLV is again visible in the both turbulence intensity and vorticity plots. The vorticity peak of the INV has now decreased beyond the cutoff value of -1 and is therefore not shown anymore. The WLV and OFV/ONV/WTV have rotated almost 270° around their roll–up center since $x^* = 0.37$.

Looking at the development from $x^* = 0.37$ downstream, the vorticity peaks for most vortices
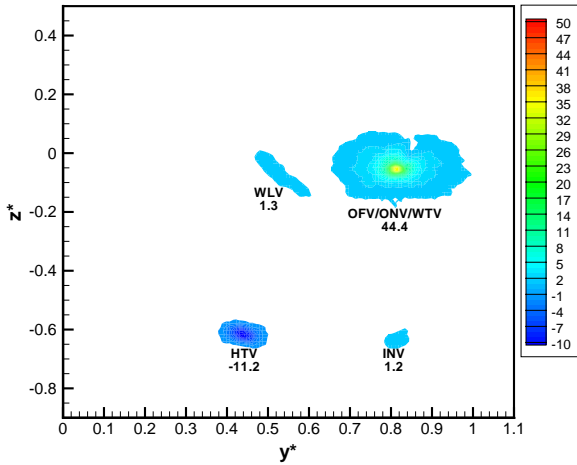
Fig. 17 Vorticity distribution for the configuration with the new Winglet at $x^* = 4.00$
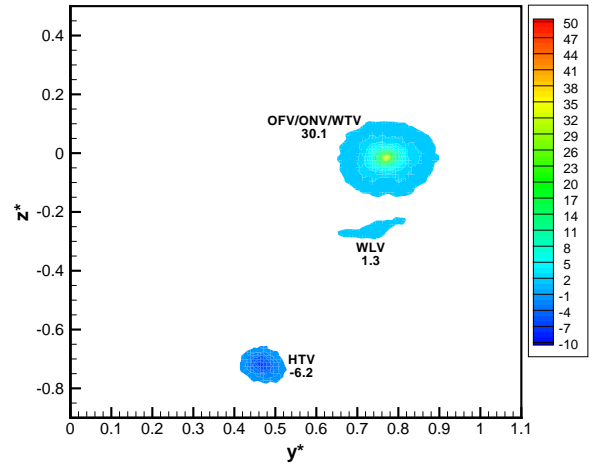
Fig. 19 Vorticity distribution for the configuration with the new Winglet at $x^* = 5.60$
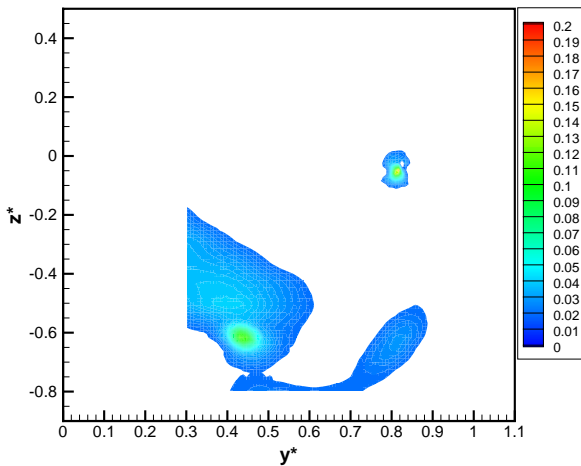
Fig. 18 Tu_z distribution for the configuration with the new Winglet at $x^* = 4.00$
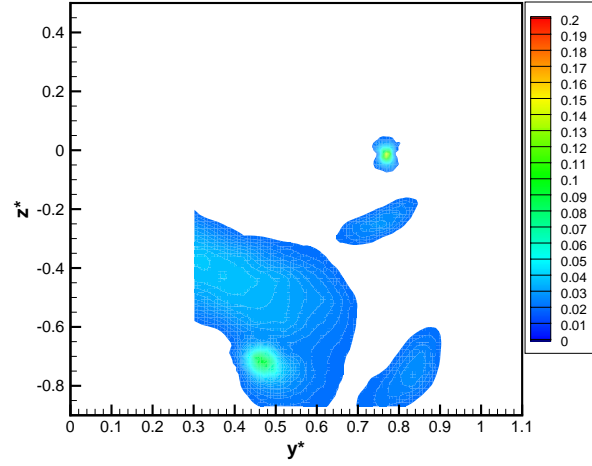
Fig. 20 Tu_z distribution for the configuration with the new Winglet at $x^* = 5.60$

decay approximately to half the value from plane to plane, except for the OFV/ONV/WTV, which decays far slower.

Comparing the measuring planes at $x^* = 5.60$ for the baseline configuration and the configuration with new winglet, a slightly different result has developed. For both configurations three vortices remained. The WLV is far weaker and smaller for the configuration with new winglet as for the baseline configuration, which is probably due to the case that the WTV is fed into the WLV for the baseline configuration, causing a higher vorticity peak from the beginning, whereas for the configuration with new winglet the WTV is

fed into the OFV/ONV. This assumption is also supported by the fact, that the OFV/ONV/WTV has a higher vorticity peak than the OFV/ONV of the baseline configuration, although the vorticity peaks for the OFV and ONV were higher for the baseline configuration at $x^* = 0.37$. The vorticity peak for the HTV is in the same magnitude for both configurations. The vortices have also rotated further around their roll–up center for the baseline than for the configuration with new winglet. For the turbulence intensity distribution a similar picture as for the baseline configuration is present.

3.2 Results with Passive Influencing

With asymmetrical deflections the lift and pitching moment coefficients stay almost constant, only the drag coefficient increases, whereas for the symmetrical deflection all three coefficients vary. The winglet is intended for active influencing in later investigations, where this is an important issue, as the horizontal tail plane can not be moved at such high frequencies as planned for the winglet tabs, in order to keep the aircraft in a steady flight condition

In order to see the influence of the tabs, measurements were performed with static deflections of the tabs to their maximum deflection angle of $\delta = 20^o$ both symmetrical and asymmetrical. Only the planes at $x^* = 0.37$ and $x^* = 5.60$ were measured and compared with the result obtained for the configuration with the new winglet without deflection. Four cases are examined as stated in Table 2. Note, that the deflection direction of the lower tab provides the case name.

Case name	δ_{lower}	δ_{upper}
symmetrical inboard	-20°	-20°
symmetrical outboard	$+20^o$	$+20^o$
asymmetrical inboard	-20°	$+20^o$
asymmetrical outboard	$+20^o$	-20°

Table 2 Examined cases with passive influencing

3.2.1 Results in the Plane at $x^* = 0.37$

Figure 21 shows the vorticity distribution for the case with symmetrical inboard deflection ($\delta_{upper} = -20^o$, $\delta_{lower} = -20^o$) at $x^* = 0.37$.

The WLV has a significantly higher vorticity peak than without deflection and the vortex distribution in the area of the winglet has changed. The WTV is connected to the WLV, which can also be seen in the turbulence intensity distribution. Comparing Figure 22 with Figure 10 clearly illustrates this connection, that the WTV and WLV will join, rather than the WTV joining the OFV/ONV. The tilted vorticity part in Figure 9 is almost completely vanished for the symmetrical inboard case. The vorticity peaks for the
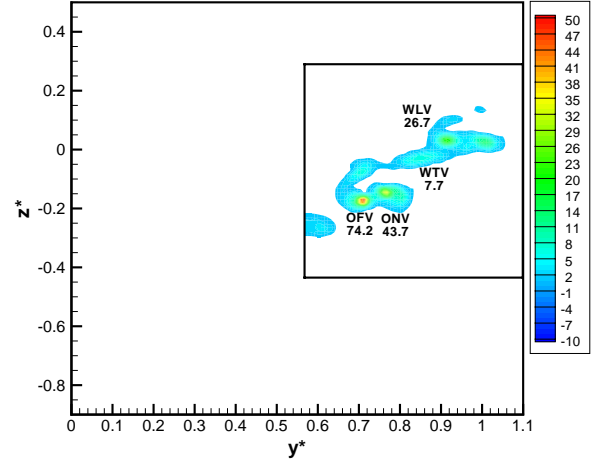
Fig. 21 Vorticity distribution for the configuration with the new Winglet at $x^* = 0.37$ with $\delta_{upper} = -20^o$ and $\delta_{lower} = -20^o$

ONV and OFV are increased. This is the case for all measurements with deflected winglet tabs.
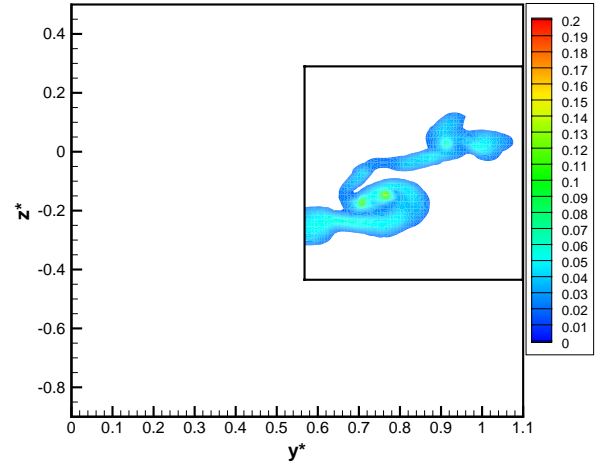
Fig. 22 Tu_z distribution for the configuration with the new Winglet at $x^* = 0.37$ with $\delta_{upper} = -20^o$ and $\delta_{lower} = -20^o$

The symmetrical outboard deflection case is illustrated in Figure 23 and 24.

The vorticity peak of the WLV is reduced to a value, which is a little lower than for the undeflected case. The WTV is in the magnitude of the reference case. In Figure 24 the vortices in the region of the winglet do not appear as stretched as for the symmetrical inboard case. The turbulence intensity field also shows a connection of

at $x^* = 0.37$ the vorticity distribution and turbulence intensities are shown in Figure 25 and 26, respectively.
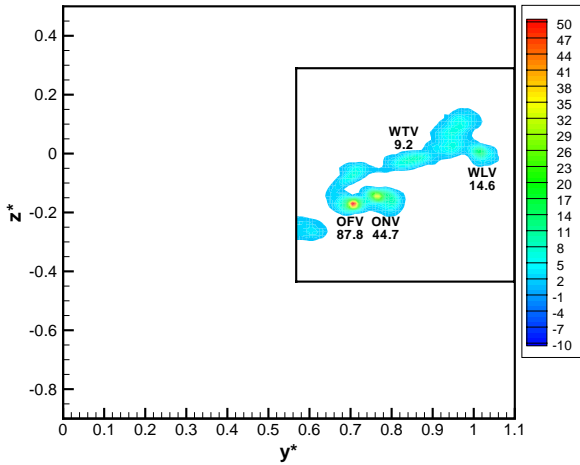
Fig. 23 Vorticity distribution for the configuration with the new Winglet at $x^* = 0.37$ with $\delta_{upper} = +20^o$ and $\delta_{lower} = +20^o$

Fig. 24 Tu_z distribution for the configuration with the new Winglet at $x^* = 0.37$ with $\delta_{upper} = +20^o$ and $\delta_{lower} = +20^o$
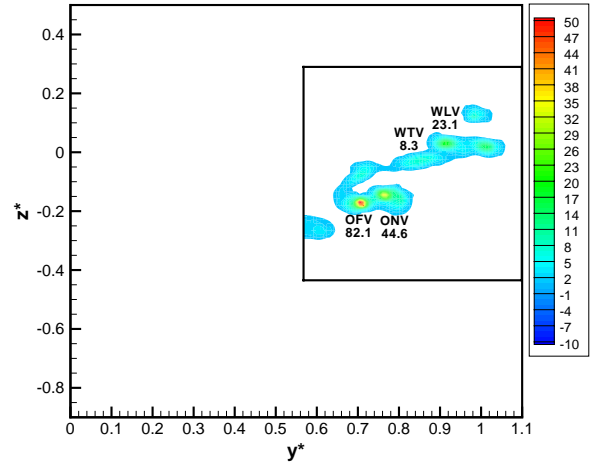
Fig. 25 Vorticity distribution for the configuration with the new Winglet at $x^* = 0.37$ with $\delta_{upper} = +20^o$ and $\delta_{lower} = -20^o$
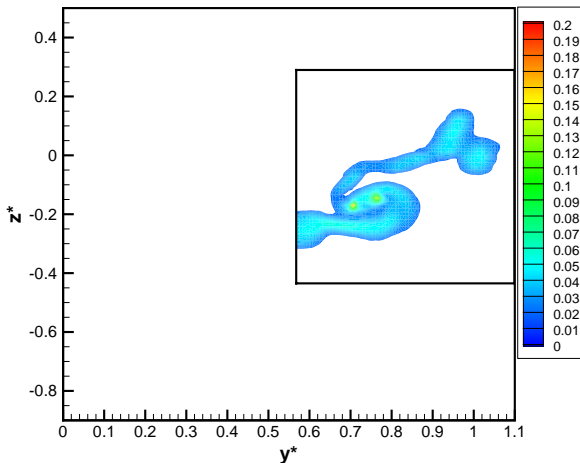
Fig. 26 Tu_z distribution for the configuration with the new Winglet at $x^* = 0.37$ with $\delta_{upper} = +20^o$ and $\delta_{lower} = -20^o$

the WTV to the WLV. Here, the OFV shows the highest vorticity peak of all deflected tab cases, which is 57% higher than for the reference case. For the symmetrical outboard case the tilted vorticity part belonging to the winglet is broadened significantly in comparison to the configuration without tab deflection. In the case of symmetrical inboard deflection this region disappeared. This is due to the winglet having an angle of incidence and the tab deflection therefore diminishing or enforcing this layer.

Continuing to the asymmetrical inboard case
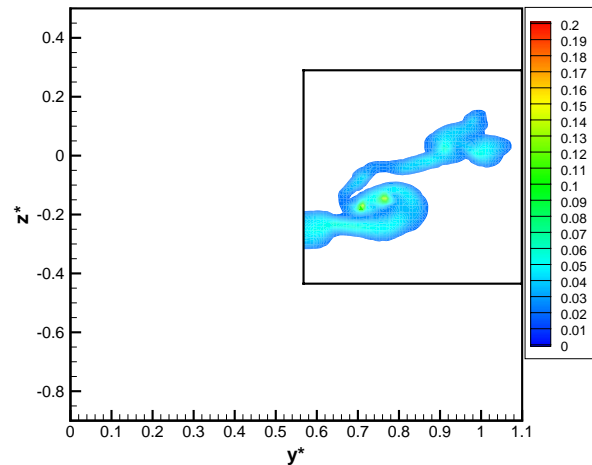
As for the symmetrical inboard deflection, the WLV has a higher vorticity peak than for the configuration without deflection and the distribution of the vortices is similar than for the symmetrical inboard case. Also the WTV is connected to the WLV, as in all other deflection cases, but opposed to the non–deflected case. Differences can

be noticed in the turbulence intensity distribution, where the positive deflected upper winglet tab causes a broadening of the turbulence layer emanating from the wing, which is visible as an additional bump in Figure 26 in comparison to Figure 10.

Inverting the tab deflection leads to the asymmetrical outboard case, illustrated in Figures 27 and 28.
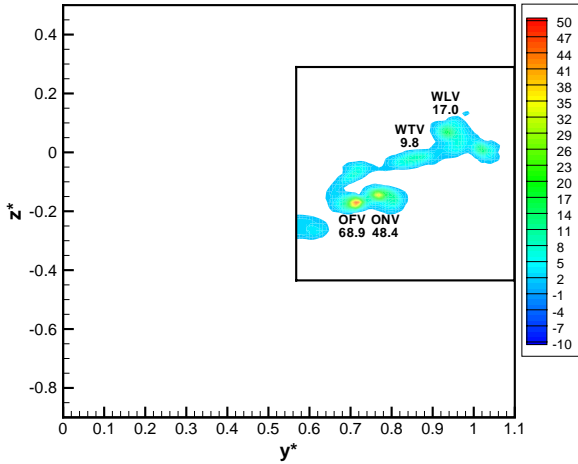
Fig. 27 Vorticity distribution for the configuration with the new Winglet at $x^* = 0.37$ with $\delta_{upper} = -20^o$ and $\delta_{lower} = +20^o$
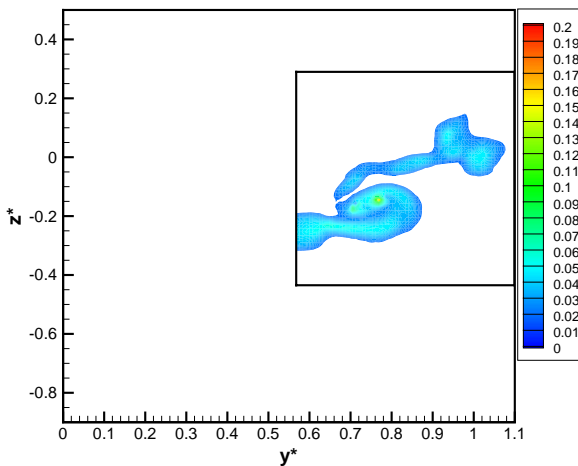
Fig. 28 Tu_z distribution for the configuration with the new Winglet at $x^* = 0.37$ with $\delta_{upper} = -20^o$ and $\delta_{lower} = +20^o$

Both the WLV and the WTV have approximately the same vorticity peak as for the symmet-

rical outboard case, which is slightly lower than for the configuration without deflected winglet tabs. The turbulence intensity distribution again shows an improved connection of the WTV to the WLV, as for the previously discussed tab deflection cases. For the asymmetrical outboard deflection case the ONV shows the highest vorticity peak of all measuremets with deflected tabs. Just as for the case with symmetrical outboard deflection the vortices in the winglet region seem to be squeezed together.

The lower tab seems to influence the vortex formation in the plane $x^* = 0.37$ far more than the upper. In all cases the OFV and the ONV showed higher vorticity peaks as the configuration without tab deflection. The WLV shows higher vorticity peak values for the inboard deflection cases and lower ones for the outboard cases. The WTV shows lower vorticity peaks in all cases, but the decrease in vorticity is more obvious for the inboard cases.

3.2.2 Results in the Plane at $x^* = 5.60$

Figure 29 shows the vorticity distribution for the case with symmetrical inboard deflection ($\delta_{upper} = -20^o$, $\delta_{lower} = -20^o$) at $x^* = 5.60$ and Figure 30 the turbulence intensity field.
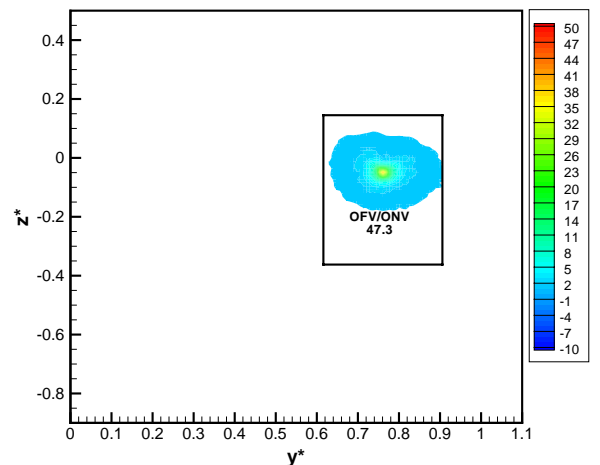
Fig. 29 Vorticity distribution for the configuration with the new Winglet at $x^* = 5.60$ with $\delta_{upper} = -20^o$ and $\delta_{lower} = -20^o$

The WLV is not evident in Figure 29, whereas it is still present in Figure 19. The remaining vor-

12
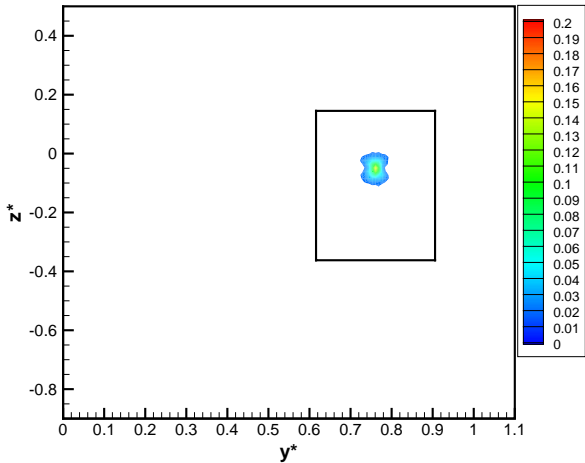
Fig. 30 Tu_z distribution for the configuration with the new Winglet at $x^* = 5.60$ with $\delta_{upper} = -20^o$ and $\delta_{lower} = -20^o$
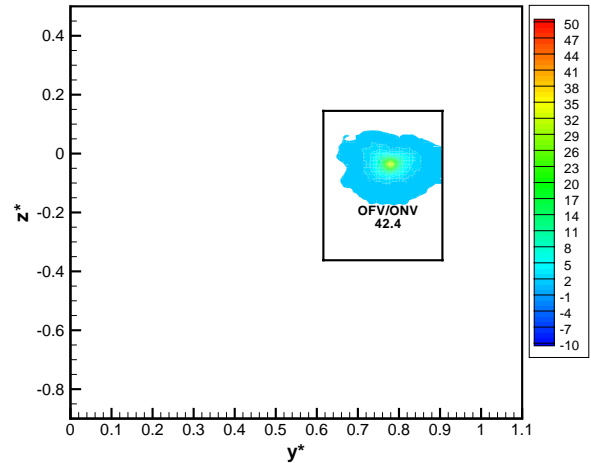
Fig. 31 Vorticity distribution for the configuration with the new Winglet at $x^* = 5.60$ with $\delta_{upper} = +20^o$ and $\delta_{lower} = +20^o$

tex, which is called OFV/ONV, as the merging of the WTV and WLV can not be proven as measurements in planes between $x^* = 0.37$ and $x^* = 5.60$ were not performed. As the vorticity peak is significantly higher (57%) for this remaining vortex as for the configuration without tab deflection, it is thought, that the WTV and WLV have merged with the OFV/ONV. The shape and size of the vortex does not differ from the reference configuration neither in vorticity nor turbulence intensity distribution.

The symmetrical outboard deflection case is illustrated in Figure 31 and 32.

This case is quite similar to the symmetrical inboard case. Again the WLV is not evident and the vorticity peak of the remaining vortex is 41% higher than for the configuration without tab deflection. The shape and size of the vortex only differs slightly from the reference configuration result.

Continuing to the asymmetrical inboard case at $x^* = 5.60$ the vorticity distribution and turbulence intensity are shown in Figure 33 and 34, respectively.

Again the WLV is not present and the vorticity peak of the remaining vortex is increased by 54% in comparison to the non–deflected case. The shape and size of the vortex is similar to the reference configuration, but the turbulence inten-
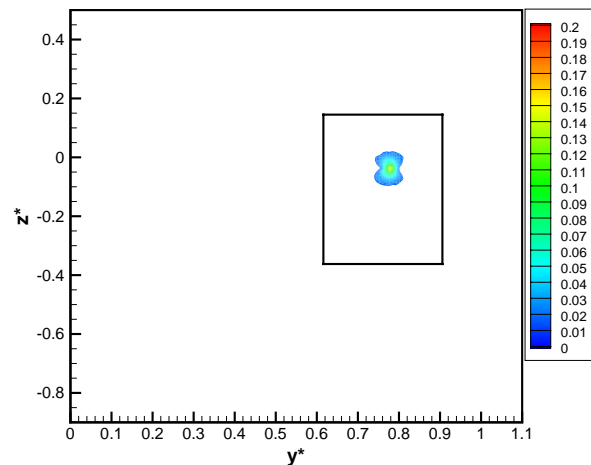
Fig. 32 Tu_z distribution for the configuration with the new Winglet at $x^* = 5.60$ with $\delta_{upper} = +20^o$ and $\delta_{lower} = +20^o$

sity distribution shows an increased turbulence level in the core of the vortex.

Inverting the tab deflection leads to the asymmetrical outboard case, illustrated in Figures 35 and 36.

The WLV is again not existent and the vorticity peak of the remaining vortex is increased by 46% in comparison to the reference configuration. The shape and size of the vortex is similar to the reference configuration, but the turbulence intensity distribution shows an increased turbulence level, which is even higher than in the pre-
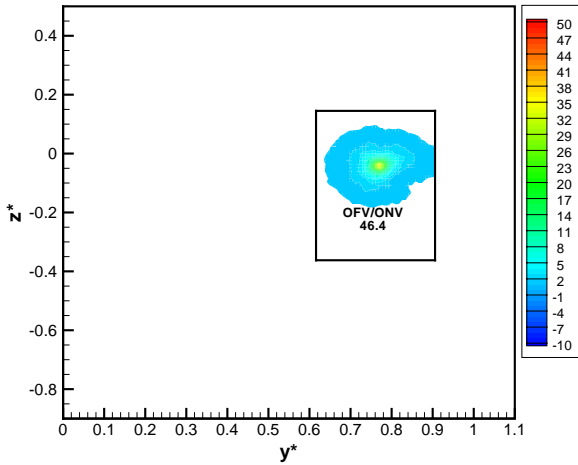
Fig. 33 Vorticity distribution for the configuration with the new Winglet at $x^* = 5.60$ with $\delta_{upper} = +20^o$ and $\delta_{lower} = -20^o$
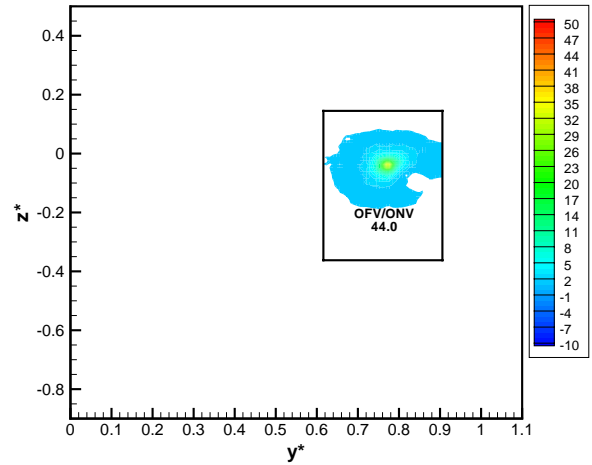
Fig. 35 Vorticity distribution for the configuration with the new Winglet at $x^* = 5.60$ with $\delta_{upper} = -20^o$ and $\delta_{lower} = +20^o$
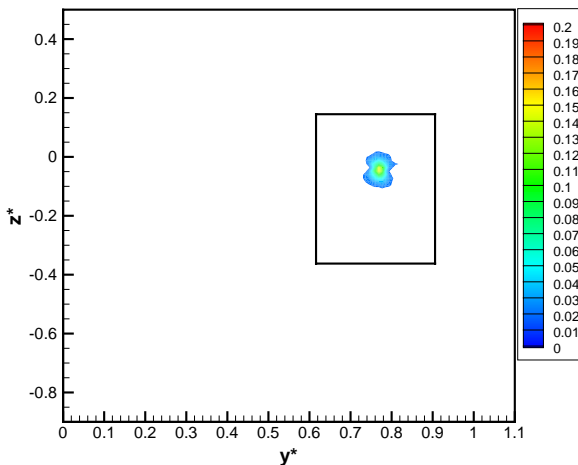
Fig. 34 Tu_z distribution for the configuration with the new Winglet at $x^* = 5.60$ with $\delta_{upper} = +20^o$ and $\delta_{lower} = -20^o$
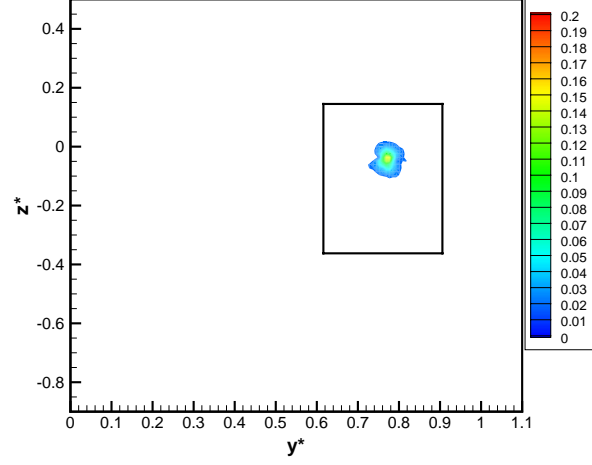
Fig. 36 Tu_z distribution for the configuration with the new Winglet at $x^* = 5.60$ with $\delta_{upper} = -20^o$ and $\delta_{lower} = +20^o$

vious case.

In the plane at $x^* = 5.60$ the cases with asymmetrical tab deflection show increased turbulence levels in the vortex core, whereas the symmetrical cases show hardly any difference to the configuration without tab deflection in means of turbulence intensity. All cases lack the presence of the WLV and probably therefore show higher vorticity peak values than for the reference case.

4 Conclusion and Outlook

An experimental investigation on the wake vortex development of a large transport aircraft in landing configuration was performed analyzing vorticity and turbulence intensity distributions in the near and extended near field. The maximum distance inspected was 5.6 spans downstream of the half model used for the wind tunnel tests. The study concentrates on the behaviour of the major vortices for an original winglet and a new winglet with tabs. The developing vortices for

14

the new winglet behaved slightly different than for the original winglet with the main difference being the vorticity peaks.

The impact of passive influencing through tabs at the trailing edge of the winglet was discussed. Four different cases, symmetrical and asymmetrical, were investigated and differences between both the cases and the baseline were observed, mainly showing increased turbulence levels for the asymmetrical cases.

In future investigations the tabs will be used actively to influence the wake vortex development. The deflection angle will be varied ($\delta = 5^o$, 10°, 20°) as well as the frequency ($f = 0 \div 100Hz$).

References

[1] C. Breitsamter, C. Bellastrada, and B. Laschka. Investigations on the turbulent wake vortex flow of large transport aircraft. In *ICAS International Congress of the Aeronautical Sciences*, pages 382.1–382.13, 2002.

[2] F. Brenner. Air Traffic Control procedures for the avoidance of wake vortex encounters: today and future developments by Deutsche Flugsicherung GmbH. In *The Characterisation & Modification of Wakes from Lifting Vehicles in Fluids, AGARD–CP–584*, pages 4–1–4–14, Trondheim, Norway, May, 1996.

[3] D. Fabre and L. Jacquin. Stability of a four–vortex aircraft wake model. *Physics of Fluids*, 12(10):4238–4243, 2000.

[4] T. Gerz, F. Holzäpfel, and D. Darracq. *Aircraft wake vortices – a position paper –*. WakeNet – the European Thematic Network on Wake Vortex, 2001.

[5] H. W. M. Hoeijmakers. Vortex wakes in aerodynamics. In *The Characterisation & Modification of Wakes from Lifting Vehicles in Fluids, AGARD–CP–584* , pages 1–1–1–12, Trondheim, Norway, May, 1996.

[6] K. Hünecke. Structure of a transport aircraft–type near field wake. In *The Characterisation & Modification of Wakes from Lifting Vehicles in Fluids, AGARD–CP–584*, pages 5–1–5–9, Trondheim, Norway, May, 1996.

[7] S. Kauertz and G. Neuwerth. Nachlauf-beeinflussung eines Tragflügels durch aktive Winglets. In *DGLR-Symposium Nachbar Flughafen*, pages 1–9, Bremen, Germany, Oct., 2004.

[8] J. M. Ortega, R. L. Bristol, and Ö. Savas. Wake alleviation properties of triangular–flapped wings. *AIAA Journal*, 40(4):709–721, 2002.

[9] E. Özger, I. Schell, and D. Jacob. On the structure and attenuation of an aircraft wake. *Journal of Aircraft*, 38(5):878–887, 2001.

[10] S. C. Rennich and S. K. Lele. Method for accelerating the destruction of aircraft wake vortices. *Journal of Aircraft*, 36(2):398–404, 1999.

[11] P. R. Spalart. Airplane trailing vortices. *Annual Review of Fluid Mechanics*, 30:107–138, 1998.